RSC Advances

PAPER

View Article Online
View Journal | View Issue

Cite this: *RSC Adv.*, 2025, **15**, 43304

Resistance components of liquid thermoelectric converter composed of $[Fe(CN)_6]^{3-}/[Fe(CN)_6]^{4-}$ aqueous electrolyte and graphite-dispersing electrodes

Soshi Fukuda[a] and Yutaka Moritomo *[abc]

Received 18th September 2025
Accepted 30th October 2025

DOI: 10.1039/d5ra07066j

rsc.li/rsc-advances

Liquid thermoelectric converter (LTE) converts environmental heat into electric power *via* the electrochemical Seebeck coefficient α. Here, we systematically investigated components of device resistance R, *i.e.*, solute (R_s), charge-transfer (R_{ct}), and diffusion (R_{dif}) resistances, of LTE composed of 0.8 M $Na_4[Fe(CN)_6]/K_3[Fe(CN)_6]$ aqueous electrolyte and graphite-dispersing electrodes. R_{ct}^{-1} and R_{dif}^{-1} linearly increase with t in the thin t region ($t \leq 40$ μm) reflecting the increase in electrochemical active surface area (EASA). The maximum power W_{max} of the ferro/ferri LTE ($t = 97$ μm) reaches 0.76 W m^{-2} at $\Delta T = 50$ K, suggesting the effectiveness of the graphite-dispersing electrode in ferro/ferri LTE.

1 Introduction

Recently, energy harvesting devices are intensively investigated from the viewpoint of achieving sustainable development goals (SDGs). Among the devices, liquid thermoelectric converter (LTE)[1–5] has simple device structure and is composed of electrolyte containing a redox couple and two identical electrodes. In addition, LTE is composed of low cost materials and is suitable for a widely used energy harvester. The LTE utilizes the thermogalvanic effect (electrochemical Seebeck coefficient α) at each electrode to convert temperature differences ΔT between the electrodes into the electromotive force V. The research of LTE is increasingly active with significant progresses.[6–25] The performance of LTE is determined by α, electric conductivity σ, and thermal conductivity κ. The maximum (W_{max}) of power is expressed as $W_{max} = \frac{\alpha^2 \Delta T^2}{4R}$, where ΔT and R is the temperature difference between the electrodes and device resistance, respectively. To increase W_{max}, it is necessary to reduce R or increase α. R can be decomposed into solution resistance R_s, charge transfer resistance R_{ct}, and diffusion resistance R_{dif}.[26]

The LTE composed of aqueous solution containing $[Fe(CN)_6]^{4-}/[Fe(CN)_6]^{3-}$ (ferro/ferri LTE) or Fe^{2+}/Fe^{3+} (Fe^{2+}/Fe^{3+}LTE) is extensively investigated because the solution is stable and exhibits rather high α. α is -1.42 mV K^{-1} for ferro/ferri LTE and 1.76 mV K^{-1} for Fe^{2+}/Fe^{3+}LTE.[9] Kim *et al.*[11] reported that addition of organic solvent in ferro/ferri LTE significantly increases α. Tanaka *et at.*[17] performed a systematic investigation on the additive effect in ferro/ferri LTE and ascribed the effect to precipitation of $K_4[Fe(CN)_6]$. On the other hand, Yu *et al.*[8] reported that addition of guanidinium in ferro/ferri LTE significantly increases α at 0.4 M from -1.4 mV K^{-1} to -3.73 mV K^{-1}. Buckingham *et al.*[21] demonstrated that α of Fe^{2+}/Fe^{3+} LTE can be optimized by pH of the electrolyte. Li *et al.*[25] reported that addition of $HClO_4$ significantly increases α and σ in Fe^{2+}/Fe^{3+} LTE. They interpreted the enhancement in terms of the formation of hexaaqua iron (III/II) complexes *via* variation of pH of the electrolyte.

To realize practical applications in society, it is necessary not only to increase W_{max} but also to reduce the costs of manufacturing elements. The coated electrodes used in ion secondary batteries are not only low cost but can also be made large and mass-produced by utilizing printing technology. Recently, Aiba *et al.*[27] demonstrated that graphite-dispersed coated electrodes significantly enhance W_{max} of Fe^{2+}/Fe^{3+} LTE. They further investigated resistance components against electrode thickness t and found that R_{ct}^{-1} and R_{dif}^{-1} linearly increase with t in the thin t region ($t \leq 80$ μm). Here, we will investigate the effectiveness of the graphite-dispersing electrode for the ferro/ferri LTE.

R of LTE can be decomposed into R_s, R_{ct}, and R_{dif}.[26–28] R_s is proportional to the electrode distance d because it is determined by the balance between the electrostatic force and frictional force acting on a moving ion.[29] R_{ct} is governed by the redox reaction rate k at the electrode surface and is independent of d. k is expressed as $k \propto \exp\left(-\frac{e\Delta E}{k_B T}\right)$, where ΔE ($= E - E_{eq}$; E and E_{eq} are the electrode and equilibrium potentials, respectively) and k_B are the overpotential and Boltzmann constant,

[a]*Graduate School of Pure & Applied Science, University of Tsukuba, Tennodai 1-1-1, Ibaraki, Tsukuba, 305-8571, Japan. E-mail: moritomo.yutaka.gf@u.tsukuba.ac.jp*
[b]*Faculty of Pure & Applied Science, University of Tsukuba, Tennodai 1-1-1, Ibaraki, Tsukuba, 305-8571, Japan*
[c]*Tsukuba Research Center for Energy Materials Science (TREMS), University of Tsukuba, Ibaraki, Tsukuba, 305-8571, Japan*

respectively. k is proportional to the electrochemical active surface area (EASA), which is usually evaluated by the magnitude of the electric double layer capacitance C_d.[31–33] In the region of $\Delta E \ll \frac{k_B T}{e}$, the charge-transfer current J_{ct} is expressed as $J_{ct} = \frac{i_0 e}{k_B T}\Delta E$,[26] where i_0 is the exchange current. On the other hand, R_{dif} is governed by diffusion of reactants and/or products driven by the concentration gradient within the diffusion layer. When a constant current is applied to a LTE, the diffusion layer gradually forms due to the redox reaction at the electrode surface. In other words, R is essentially $R_s + R_{ct}$ immediately after the current apply, because there exits neither diffusion layer nor diffusion. When enough time has passed, the system reached a steady state with a steady diffusion layer, which drives mass transfer equal to the redox reaction rate at the electrode surface. In the steady state, R is expressed as $R_s + R_{ct} + R_{dif}$. In other words, R_{dif} can be evaluated by subtracting $R_s + R_{ct}$ from R in the steady state. Importantly, R_{dif} is directly related to the finite diffusion impedance $Z_W^f = \left[\frac{A_W}{\sqrt{2i\omega}}\tanh\left(\sqrt{\frac{i\omega}{D}}\delta\right)\right.$; where A_W, ω, δ, and D are the Warburg coefficient, angular velocity, thickness of the diffusion layer, and diffusion constant, respectively].[30] At low frequency limit ($\omega \to 0$), Z_W^f converges a constant value $\left(\mathrm{Re}Z_W^f \to A_W\frac{\delta}{\sqrt{2D}}\text{and } \mathrm{Im}Z \to 0\right)$. R_{dif} corresponds to the low frequency limit of $\mathrm{Re}Z_W^f = \left(A_W\frac{\delta}{\sqrt{2D}}\right)$.

In this paper, we investigated the resistivity components in ferro/ferri LTE composed of graphite-dispersing electrodes against t. In particular, R_{dif} was evaluated using two methods, *i.e.*, subtraction of $R_s + R_{ct}$ from R and analysis by Randles equivalent circuit including Z_W^f. Low frequency electrochemical impedance spectroscopy (EIS) reveals that mass transfer process is the main rate-limiting factor in ferro/ferri LTE.

2 Experimental section

2.1 Coated electrode and electrolyte

The graphite-dispersing coated electrode was prepared as described in literature.[27,28] The graphite powder and polyvinylidene difluoride (PVDF) were mixed thoroughly in a weight ratio of 9 : 1 with *N*,*N*-dimethylformamide (DMF). Graphite powder (CAS RN: 7782-42-5, Wako Special Grade) was purchased from FUJIFILM Wako corp. and used as received. The mixture was coated onto a stainless-steel foil (SUS304, 10 μm) with use of an applicator, and was dried in vacuum at 60 °C. The electrode thickness t, which was controlled by the height of the applicator, was evaluated with a digital micrometer.

The electrolyte was aqueous solutions containing 0.8 M $Na_4[Fe(CN)_6]$ and 0.8 M $K_3[Fe(CN)_6]$. The reason for choosing $Na_4[Fe(CN)_6]$ rather than $K_4[Fe(CN)_6]$ is the higher solubility of the former. The solutes were purchased from FUJIFILM Wako corp. and used as received. The solute concentration (=0.8 M) was the same as in the literature,[27] because W_{max} of aqueous LTE increases with solute concentration.[9]

2.2 Fabrication of LTE

Resistance components and output characteristics of LTE were investigated with a specially designed two-pole cell.[34] The cell consists of a cylindrical electrolyte tank and two aluminum bases. The electrolyte tank was a 7.3 mm ϕ polytetrafluoroethylene (PTFE) cylinder, whose ends were sealed with the bases. The inner surfaces of the bases were completely covered with the graphite-dispersing electrodes or commercially available graphite sheets (GS; t = 220 μm). The electrode distance d and area s were 10 mm and 42 mm^2, respectively. Temperatures of the high (T_H) and low (T_L) electrodes were monitored with T-type thermocouples and independently controlled with a Peltier element equipped with a heat sink and a cooling fan, which were attached to the outer surfaces of the bases. ΔT is defined by $\Delta T = T_H - T_L$.

2.3 Device resistance and resistance components

Device resistance R was evaluated from current I–voltage V relation at 298 K (ΔT = 0 K). I was changed stepwisely. The V value at each I was measured after waiting several minutes until the time change of V almost disappeared. Measurements were performed with horizontally orientated LTE. The slope of the I–V plot corresponds to R.

Resistance components, *i.e.*, R_s, R_{ct} and R_{dif}, were evaluated by electrochemical impedance spectroscopy (EIS) with use of a potentiostat (Vertex.one.EIS, Ivium technologies) at 298 K (ΔT = 0 K). The whole measurements were performed with horizontally orientated LTE. No diffusion layer is formed in the fast f region ($f \geq$ 1Hz) while its effects begin to appear in the slow f region (∼mHz). In the usual case, the frequency f of the alternative electric field was from 1 Hz to 20 kHz and the amplitude was 10 mV. The obtained EIS data ($f \geq$ 1Hz) were analyzed with a Randles equivalent circuit composed of R_s, R_{ct}, C_d, and Warburg impedance $Z_W = \left(\frac{A_W}{\sqrt{2i\omega}}\right)$, as shown in Fig. 1(a). R_{dif} was evaluated by subtracting $R_s + R_{ct}$ from R. Hereafter, thus evaluated value will be referred to as R'_{dif} to distinguished it from R_{dif} evaluated directly by EIS measurements.

To evaluate R_{dif} from EIS measurements, we further performed EIS measurement in an expanded f range from 1 m Hz to 25 kHz at 298 K. The amplitude was 10 mV. The obtained EIS data (≥1 mHz) were analyzed with a Randles equivalent circui composed of R_s, R_{ct}, C_d, and Z_W^f, as shown in Fig. 1(b). At low frequency limit ($\omega \to 0$), Z_W^f converges a constant value $\left(\mathrm{Re}Z_W^f \to A_W\frac{\delta}{\sqrt{2D}}\text{ and } \mathrm{Im}Z \to 0\right)$. R_{dif} corresponds to the low frequency limit of $\mathrm{Re}Z_W^f = \left(A_W\frac{\delta}{\sqrt{2D}}\right)$.

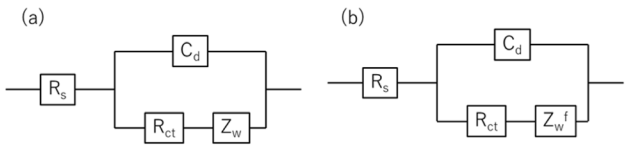

Fig. 1 (a) Randles equivalent circuit composed of R_s, R_{ct}, C_d, and Z_W. (b) Randles equivalent circuit composed of R_s, R_{ct}, C_d, and Z_W^f.

2.4 Output characteristics of LTE

Output characteristics of LTE were investigated at $T_L = 300$ K and $T_H = 330$ K ($\Delta T = 30$ K). The V value was measured against current I. I was changed stepwisely. The V value at each I was measured after waiting a few minutes until the time change of V almost disappeared. The power W is expressed as $W = IV$. The open-circuit voltage V_0 and R were evaluated by least-squares fitting of the I–V plot with $V = V_0 + IR$. W_{max} is expressed as $W_{max} = \frac{{V_0}^2}{4R}$.

3 Results and discussion

3.1 Resistance components against electrode thickness t

Fig. 2 shows current I–voltage V plot of the ferro/ferri LTEs, which are composed of 0.8 M $Na_4[Fe(CN)_6]$ and 0.8 M $K_3[Fe(CN)_6]$ aqueous solution and graphite-dispersing electrode, at 298 K against t. s and d were 42 mm^2 and 10 mm, respectively. At all temperatures, V increases in proportion to I. R was evaluated from the slope of the plot, as indicated by straight lines. With increase in t, R gradually decreases from 40.8 Ω at $t = 27$ μm to 22.4 Ω at 72 μm. With further increase in t, R slightly increases to 25.8 Ω at 81 μm and 24.0 Ω at 113 μm. Above $t \geq 40$ μm, R becomes comparable with R of the LTE composed of GS.

Fig. 3 shows Nyquist plots of complex impedance of the ferro/ferri LTEs at 298 K at different t. s and d were 42 mm^2 and 10 mm, respectively. The vertical axis is shifted for each plot. The Nyquist plot at 27 μm shows a prototypical shape. The plot shows a semicircle at the left side and a straight line with an inclination of 45° at the right side. The resistances at the left and right sides of the semicircle correspond to R_s and $R_s + R_{ct}$, respectively. Solid curves are the results of least-squares fits with a Randles equivalent circuit composed of R_s, R_{ct}, C_d, and Z_W [Fig. 1(a)]. Feature of the observed impedance is well reproduced by the equivalent circuit. Similar behaviors are observed in the other Nyquist plots. R_s, R_{ct}, C_d, and A_W were evaluated against t by least-squares fits with the Randles equivalent circuit We attempted to evaluate the parameters for GS, but was unable to obtain reliable values. We further evaluated R'_{dif} by subtracting $R_s + R_{ct}$ from R.

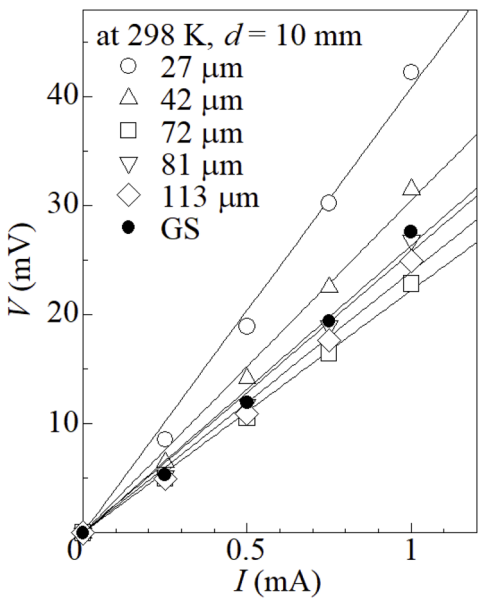

Fig. 2 Voltage V against current I of LTEs composed of 0.8 M $Na_4[Fe(CN)_6]$ and 0.8 M $K_3[Fe(CN)_6]$ aqueous solution and graphite-dispersing electrodes at 298 K at different t. s and d were 42 mm^2 and 10 mm, respectively. Filled circles are the data of LTE composed of commercially available GS ($t = 220$ μm). Straight lines are the results of least-squares fits.

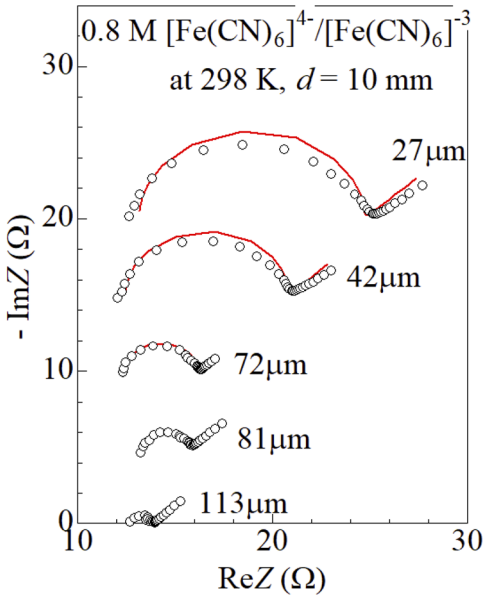

Fig. 3 Nyquist plots of complex impedance of LTEs composed of 0.8 M $Na_4[Fe(CN)_6]$ and 0.8 M $K_3[Fe(CN)_6]$ aqueous solution and graphite-dispersing electrodes at 298 K at different t. The vertical axis is shifted for each plot. s and d were 42 mm^2 and 10 mm, respectively. Solid curves are the results of least-squares fits with a Randles equivalent circuit composed of R_s, R_{ct}, C_d, and Z_W. The reliable factor $\chi^2 = \left[\sum_{i=1}^{N} \frac{(ReZ^{cal} - ReZ)^2 + (ReZ^{cal} - ReZ)^2}{ReZ^2 + ImZ^2}\right]$ was 8.5 × 10^{-4}, 5.7 × 10^{-4}, 1.6 × 10^{-4}, 1.6 × 10^{-4}, 1.1 × 10^{-4} at $t = 27$, 42, 72, 81, and 113 μm, respectively.

Fig. 4(a) shows R^{-1} of the ferro/ferri LTEs against t at 298 K. In the small t region below 40 μm, R^{-1} steeply increases with t, and then nearly saturated at ≈ 0.04 Ω^{-1}. The saturated value is almost the same as the R^{-1} value of GS. Fig. 4(b) shows R_s^{-1} against t at 298 K. R_s^{-1} (=0.076 Ω^{-1}) is almost independent d, as indicated by straight line. This is because macroscopic electric force between the electrodes is independent of the microscopic electrode structure. A similar t-independent behavior of R_s^{-1} is observed in the LTEs composed of 0.8 M $Fe(ClO_4)_2$ and 0.8 M $Fe(ClO_4)_3$ aqueous[27] or methanol solutions.[28] Fig. 4(c) shows R_{ct}^{-1} against t at 298 K. R_{ct}^{-1} linearly increases with t, as indicated by straight line. The increase can be ascribed to the increase in EASA. Fig. 4(d) shows C_d, which is a sensitive measure of EASA,[31–33] against t at 298 K. As indicated by a straight line, C_d and hence EASA linearly increases with t.

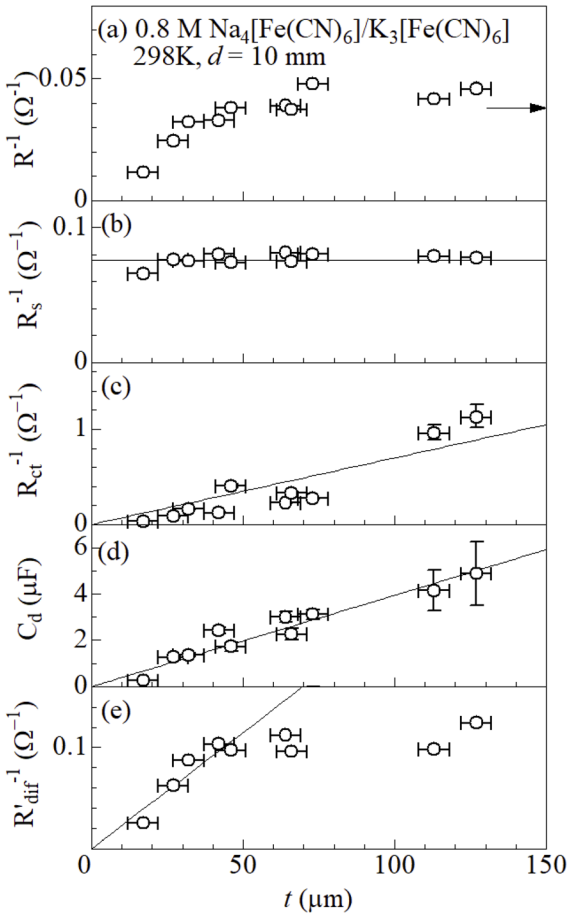

Fig. 4 (a) R^{-1}, (b) ${R_s}^{-1}$, (c) ${R_{ct}}^{-1}$, (d) C_d, and (e) ${R'_{dif}}^{-1}$ of LTEs composed of 0.8 M $Na_4[Fe(CN)_6]$ and 0.8 M $K_3[Fe(CN)_6]$ aqueous solution and graphite-dispersing electrodes against t at 298 K. s and d were 42 mm^2 and 10 mm, respectively. R'_{dif} was evaluated by subtracting $R_s + R_{ct}$ from R. A horizontal arrow in (a) indicates R^{-1} of the LTE composed of GS ($t = 220$ μm). The solid straight lines in (b), (c), (d), and (e) are results of least-squares fit. The vertical error bars are those of t. The horizontal error bars in (b). (c), and (d) were those of R_s, R_{ct}, and C_d, respectively. The errors were evaluated using equivalent circuit analyses. The horizontal error bars in (b) were smaller than the size of the symbols. The reliable factor $\chi^2 \left[= \sum_{i=1}^{N} \frac{(\mathrm{Re}Z^{cal} - \mathrm{Re}Z)^2 + (\mathrm{Re}Z^{cal} - \mathrm{Re}Z)^2}{\mathrm{Re}Z^2 + \mathrm{Im}Z^2} \right]$ was in the range of 1.1×10^{-4} to 8.5×10^{-4} except that ($=2.8 \times 10^{-3}$) at 17 μm.

Fig. 4(e) shows R'_{dif} against t at 298 K. Interestingly, ${R'_{dif}}^{-1}$ linearly increases with t in the small t region ($t \leq 40$ μm) while it becomes nearly constant in the thick t region. The increase in the thin t region is also ascribed to the increase in EASA [(e)]. Aiba *et. al.*[27] reported a similar behavior of ${R'_{dif}}^{-1}$ in Fe^{2+}/Fe^{3+} LTE. ${R'_{dif}}^{-1}$ linearly increases with t in the thin t region ($t \leq 80$ μm) and becomes nearly constant in the thick t region. The saturation is probably ascribed to restricted mass transfer in a deep region of the electrode. In the deep region, mass transfer is too slow to continue the redox reaction. In other words, the graphite particles in the deep region are electrochemically inactive at the steady state and do not contribute to the Faraday current. In this scenario, characteristic thickness (t_{ch}) where ${R'_{dif}}^{-1}$ begins to saturate corresponds to the minimum depth where graphite particles become inactive. It is reasonable that t_{ch} (=40 μm) of the ferro/ferri LTE is much smaller than t_{ch} (=80 μm) of the Fe^{2+}/Fe^{3+} LTE, because the ionic radius of ferro/ferri (~4.3 Å) is larger than that of Fe^{2+}/Fe^{3+} (~0.8 Å).

3.2 Low frequency EIS

In this subsection, we will quantitatively compare the resistance components of ferro/ferri LTE with the Fe^{2+}/Fe^{3+} LTE, which is composed of aqueous solution containing Fe^{2+}/Fe^{3+} redox couple. We note that the resistance components strongly depend not only on d and ΔT, but also on the electrolyte concentration and electrode material. To quantitatively compare the resistance components, the device parameters should be the same except for the type of solutes. We fabricated the Fe^{2+}/Fe^{3+} LTE using the same cell and electrodes as used in the ferro/ferri LTE. The electrolyte was aqueous solutions containing 0.8 M $Fe(ClO_4)_2$ and 0.8 M $Fe(ClO_4)_3$. The solutes were purchased from FUJIFILM Wako corp. and used as received.

Fig. 5 shows Nyquist plots of complex impedance of the (a) ferro/ferri and (b) Fe^{2+}/Fe^{3+} LTEs at 298 K. The frequency range was expanded from 1 mHz to 25 kHz to directly evaluate R_{dif} by least-squares fit with a Randles equivalent circuit. s and d were

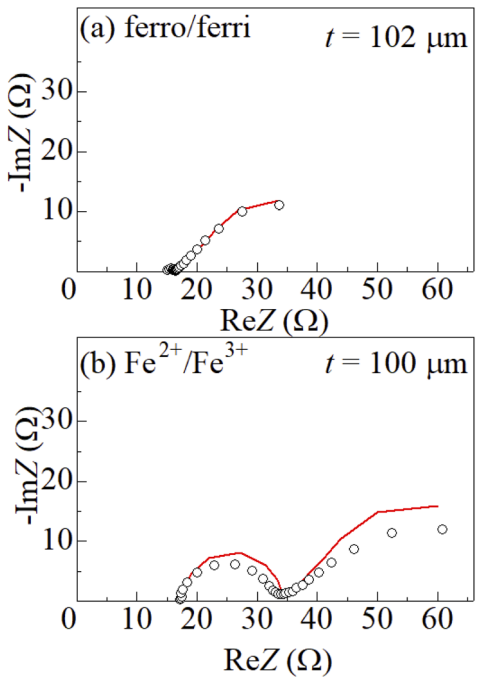

Fig. 5 Nyquist plots of complex impedance of (a) ferro/ferri and (b) Fe^{2+}/Fe^{3+} LTEs at 298 K. s and d were 42 mm^2 and 10 mm, respectively. Solid curves are the results of least-squares fits with a Randles equivalent circuit composed of R_s, R_{ct}, C_d, and $Z_W^f = \left(\frac{A_W}{\sqrt{2i\omega}}\right) \tanh Z_W^f = \left(\sqrt{\frac{i\omega}{D}}\delta\right)$, where δ, and D are the thickness of the diffusion layer and diffusion constant, respectively. The reliable factor $\chi^2 = \left[\sum_{i=1}^{N} \frac{(\mathrm{Re}Z^{cal} - \mathrm{Re}Z)^2 + (\mathrm{Re}Z^{cal} - \mathrm{Re}Z)^2}{\mathrm{Re}Z^2 + \mathrm{Im}Z^2}\right]$ was 2.9×10^{-4} and 2.0×10^{-3} for the ferro/ferri and Fe^{2+}/Fe^{3+} LTEs, respectively.

42 mm^2 and 10 mm, respectively. The Nyquist plot of the (a) ferri/ferro LTE shows a prototypical shape. In the high f region (left region), the plot shows a semicircle at the left side and a straight line with an inclination of 45° at the right side. With further decreasing f (right region), the slope gradually becomes gentler and eventually becomes almost flat. The deviation from a 45-degree straight line in the low f region can be ascribed to the formation of the diffusion layer. The overall features are reproduced by a Randles equivalent circuit composed of R_s, R_{ct}, C_d, and Z_W^f [Fig. 1(b)], as indicated by solid curves. R_s, R_{ct}, C_d, $\frac{\sqrt{2}}{A_W}$, and $\frac{\delta}{\sqrt{D}}$ were evaluated by least-squares fits with the Randles equivalent circuit and listed in Table 1. At low frequency limit ($\omega \rightarrow 0$), Z_W^f converges a constant value $\left(\mathrm{Re}Z_W^f \rightarrow A_W\frac{\delta}{\sqrt{2D}} \text{and } \mathrm{Im}Z \rightarrow 0\right)$. R_{dif} corresponds to the low frequency limit of $\mathrm{Re}Z_W^f = \left(A_W\frac{\delta}{\sqrt{2D}}\right)$ and is also listed in Table 1.

Similar behaviors are observed in (b) Fe^{2+}/Fe^{3+} LTE. In Fe^{2+}/Fe^{3+} LTE, the diameter of the semicircle is much larger than the corresponding diameter of the (a) ferro/ferri LTE. This indicates that R_{ct} of the Fe^{2+}/Fe^{3+} LTE is much larger than that of the ferro/ferri LTE. In the Fe^{2+}/Fe^{3+} LTE, the change in ReZ from the right side of the semicircle to the local maximum is ≈ 26 Ω while the corresponding change is ≈ 19 Ω in the ferri/ferro LTE. This suggests that R_{dif} of the Fe^{2+}/Fe^{3+} LTE is larger than that of the ferro/ferri LTE. The solid curve in (b) is the least-squares fitted result with a Randles equivalent circuit composed of R_s, R_{ct}, C_d, and Z_W^f. The obtained parameters were listed in Table 1. R_{ct} (=16.4 Ω) of the Fe^{2+}/Fe^{3+} LTE is much larger than that (=1.3 Ω) of the ferro/ferri LTE. R_{dif} (=39.1 Ω) of the Fe^{2+}/Fe^{3+} LTE is slightly larger than that (=28.3 Ω) of the ferro/ferri LTE. Therefore, the obtained parameters of the Fe^{2+}/Fe^{3+} LTE are reliable even though the agreement between the observed data and the calculated values is not very good.

We will compare the resistance components between the ferro/ferri and Fe^{2+}/Fe^{3+} LTEs. R_s (=15.2 Ω) of the former LTE is almost the same as that (=17.6 Ω) of the latter LTE. Interestingly, R_{ct} (=1.3 Ω) of the former LTE is much smaller than that (=16.4 Ω) of the latter LTE. This indicates that the redox reaction of $[Fe(CN)_6]^{4-}/[Fe(CN)_6]^{3-}$ is much faster than the redox reaction of Fe^{2+}/Fe^{3+}. R_{dif} (=28.3 Ω) of the former LTE is larger than that (=39.1 Ω) of the latter LTE. R_{ct} is an index of the difficulty of charge transfer at the electrode surface while R_{dif} is an index of the difficulty of mass transfer within the diffusion layer. The very small $\frac{R_{ct}}{R_{dif}}$ (=0.08) in the ferro/ferri LTE suggests that mass transfer process is the main rate-limiting factor, probably reflecting large effective ionic radius of $[Fe(CN)_6]^{4-}/[Fe(CN)_6]^{3-}$ and resultant small D. In the steady state, there are few reactants at the electrode surface, and reactants transported by diffusion react quickly. On the other hand, the rather large $\frac{R_{ct}}{R_{dif}}$ (=0.42) in the Fe^{2+}/Fe^{3+} LTE suggests both the charge and mass transfer processes play important roles in the steady state.

Finally, let us compare the diffusion resistance evaluated by two methods, *i.e.*, R_{dif} evaluated by EIS measurement and $R_{dif}^{'}$ evaluated by subtraction of $R_s + R_{ct}$ from R. In Table 1, we listed R and $R_{dif}^{'}$ ($= R - R_s - R_{ct}$). For all LTEs, $R_{dif}^{'}$ is about half of R_{dif}. This unexpected discrepancy between R_{dif} and $R_{dif}^{'}$ is understandable if we consider the frequency response of Z_W^f. At sufficiently high f region ($f \gg 1$), $\tanh\left(\sqrt{\frac{i\omega}{D}}\delta\right) \sim 1$ and hence, Z_W^f behaves the same as Z_W. As f decreases to a characteristic frequency $\left(f_{ch} = \frac{D}{\delta^2}\right)$, Z_W^f begins to deviate from Z_W. With further decrease in f, the Nyquist plot of Z_W^f show local maxima and then converges to a constant on the real axis; $\mathrm{Re}Z_W^f \rightarrow A_W\frac{\delta}{\sqrt{2D}}$ and $\mathrm{Im}Z \rightarrow 0$ when $f \rightarrow 0$. With use of the parameters shown Table 1, f_{ch} of the ferro/ferri and Fe^{2+}/Fe^{3+} LTEs are estimated to be 5 and 6 mHz, respectively. To reach the ture stady state, LTE requires times several orders of magnitude longer than $\frac{1}{f_{ch}}$ (= several minutes). In the DC current measurement, the V value at each I was carefully measured after

Table 1 Parameters of ferro/ferri and Fe^{2+}/Fe^{3+} LTEs at 0.8 M and at 298 K. *s* and *d* were 42 mm^2 and 10 mm, respectively R_s, R_{ct}, R_{dif}, C_d, A_W, and R are solution resistance, charge-transfer resistance, diffusion resistance, double-layer capacitance, Warburg coefficient, and device resistance, respectively. R_s, R_{ct}, C_d, and $\frac{\sqrt{2}}{A_W}$ were evaluated by least-squares fits with the Randles equivalent circuit composed of R_s, R_{ct}, C_d, and $Z_W^f = \left(\frac{A_W}{\sqrt{2i\omega}}\right)\tanh\left(\sqrt{\frac{i\omega}{D}}\delta\right)$, where δ, and D are the thickness of the diffusion layer and diffusion constant, respectively) with fixing $\frac{\delta}{\sqrt{D}}$ at 14 $s^{1/2}$ (ferro/ferri) or 13 $s^{1/2}$ (Fe^{2+}/Fe^{3+}). C_d of ferro/ferri LTE was fixed at 4.9 μF due to the small semiciecle. The numbers in parentheses represent the errors evaluated by equivalent circuit analysis. $R_{dif} = \left(A_W\frac{\delta}{\sqrt{2D}}\right)$ is calculated by dividing $\frac{\delta}{\sqrt{D}}$ by $\frac{\sqrt{2}}{A_W}\cdot A_W\frac{\delta}{\sqrt{2D}}$. R was evaluated by the slope of the I–V plot with use of DC current. $R_{dif}^{'}$ was evaluated by subtracting $R_s + R_{ct}$ from R

Redox couple	t (μm)	R_s (Ω)	R_{ct} (Ω)	C_d (μF)	$\frac{\sqrt{2}}{A_W}$ ($s^{1/2}$/Ω)	$\frac{\delta}{\sqrt{D}}$ ($s^{1/2}$)	R_{dif} (Ω)	R (Ω)	$R_{dif}^{'}$ (Ω)
Ferro/ferri	102	15.2(5)	1.3(5)	4.9	0.494(7)	14	28.3	28.9	12.4
Fe^{2+}/Fe^{3+}	100	17.6(5)	16.4(8)	13.3(2.0)	0.333(16)	13	39.1	52.1	18.1

waiting several minutes until the time change of V almost disappeared. Several minutes, however, is too short for the LTE to reach the true steady state. It may take a few hours or tens of hours to reach the true steady state. In other words, V and hence $R = \left(\frac{V}{I}\right)$ is tends to be underestimated in the DC current measurement even if one measures V after waiting several minutes. Actually, R is roughly the same as the real part of each Nyquist plot at several mHz, whose inverse is several minutes. This is why R'_{dif} is smaller than R_{dif}. This argument indicates that absolute value of R_{dif} is more reliable than R'_{dif}. Relative value of R'_{dif} may be reliable if $f_{ch} = \left(\frac{D}{\delta^2}\right)$) is about the same.

Fig. 6 shows time dependence of electromotive force V of ferro/ferri LTE ($t = 105$ μm) at $\Delta T = 30$ K under constant current I of 0.44 mA. In (a) short time region, V rapidly decreases in the first several ten seconds and then becomes almost constant. With further increase in time [(b)], V decreases very slowly and finally becomes constant at ~16 hours. The slow decrease in V can be ascribed slow formation of the diffusion layer, which reaches a steady-state at ~16 hours. The rapid initial voltage drop can be ascribed to depletion of the reactants from the electrode surface due to the Faraday current. Looking closely at Fig. 6(a), one may notice that V shows a local minimum at 40 seconds and then slightly increases. This slight increase is probably due to onset of the diffusion process, which may be triggered by the depletion of the reactants.

3.3 Output characteristics

Fig. 7(a) shows output characteristics of the ferro/ferri LTEs at different ΔT. d and s were 10 mm and 42 mm^2, respectively. Reflecting R, the V value linearly decreases with I as $V = V_0$–IR (solid line). In Table 2, we listed thus evaluated V_0, R, $W_{max} = \left(\frac{V_0^2}{4R}\right)$. V_0 increases almost linearly with ΔT. W_{max} is expected to increase in proportion to the square of V_0 ($=\alpha\Delta T$), and hence ΔT. As expected, W_{max} quadratically increases from 0.12 W m^{-2} at $\Delta T = 20$ K, 0.31 W m^{-2} at $\Delta T = 30$ K, 0.48 W m^{-2} at $\Delta T = 40$ K, to 0.76 W m^{-2} at $\Delta T = 50$ K. In Table 3, we compare thus obtained W_{max} with those of ferro/ferri LTEs reported in literature. We note that R strongly depend d, since R_s is proportional to d while R_{ct} and R_{dif} are independent on d.[27,28] Furthermore, W_{max} increases in proportion to is proportional to ΔT^2. Therefore, a direct comparison of W_{max} evaluated at different d and ΔT is difficult. Roughly speaking, however, W_{max} in the ferro/ferri LTE composed of the graphite-dispersing electrodes is comparable with those reported in literature.

The dimensionless figure of merit ($ZT = \frac{\alpha^2\sigma T}{\kappa}$, σ and κ are electric and thermal conductivities, respectively) is a significant parameter for thermoelectric converter, since it determines the thermal efficiency η. Unlike W_{max}, ZT does not depend on ΔT. α ($=-1.04$ mV K^{-1}) was evaluated from the slop of the ΔT – V_0 plot. $\sigma = \left(\frac{d}{sR}\right)$ was evaluated to be 0.11 S cm^{-1} using the

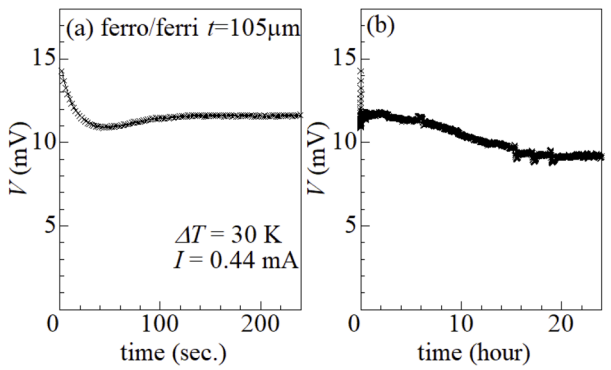

Fig. 6 Time dependence of electromotive force V of ferro/ferri LTE ($t = 105$ μm) at $\Delta T = 30$ K under constant current I of 0.44 mA; (a) short and (b) long time regions.

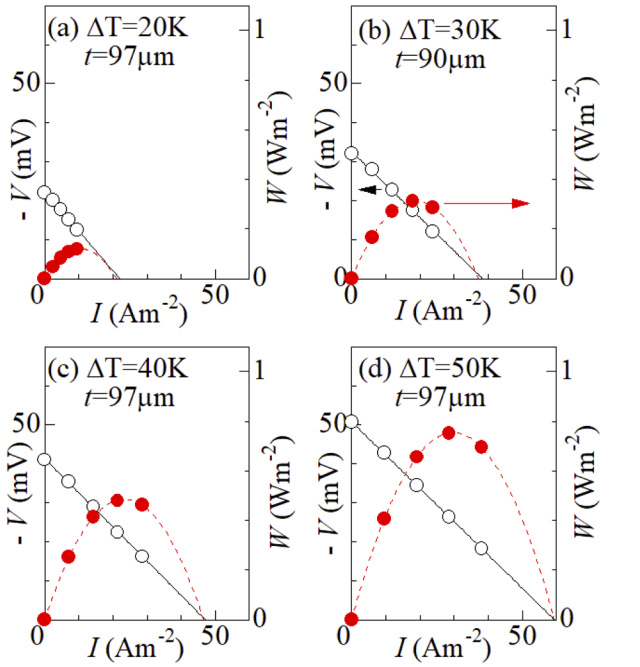

Fig. 7 Output voltage V (open circles) and power density W (filled circles) against current density I of ferro/ferri LTEs at difference ΔT: (a) 20 K, (b) 30 K, (c) 40 K, and (d) 50 K. s and d were 42 mm^2 and 10 mm, respectively. Solid straight lines are results of least-squares fits of the I–V plots. Broken curves are results of least-squares fits with quadratic function.

Table 2 Output properties of ferro/ferri LTE. ΔT, t, V_0, R, and $W_{max} = \left(\frac{V_0^2}{4R}\right)$ are the temperature difference between the hot and cold electrodes, thickness of the electrode, open-circuit voltage, device resistance, and maximum output, respectively

ΔT (K)	t (μm)	V_0 (mV)	R (mΩ m^{-2})	W_{max} (W m^{-2})
20	97	−22.3	1.01	0.12
30	90	−32.5	0.85	0.31
40	97	−41.3	0.88	0.48
50	97	−50.7	0.85	0.76

Table 3 Output characteristics of ferro/ferri LTEs. ΔT, d, s, W_{max}, $ZT = \left(\frac{\alpha^2 \sigma T}{\kappa}\right)$; σ and κ are electric and thermal conductivities, respectively), are the temperature difference, electrode distance, electrode area, maximum of output, and dimensionless figure of merit, respectively. In evaluation ZT, T was fixed at 298 K and κ was assumed to be 0.5 W Km^{-1}

ΔT (K)	d (mm)	s (mm^2)	W_{max} (W m^{-2})	ZT	References
22	20	512	0.05	0.005	8
20	5	100	0.47	0.014	9
10	15	—	0.10	0.036	10
10	10	42	0.01	0.002	17
20	10	42	0.12	0.007	This work
50	10	42	0.76	0.007	This work

average value (=0.90 Ω) of R. On the other hand, Kim *et al.*[9] reported κ of aqueous solution containing x M $K_4[Fe(CN)_6]$ and x M $K_3[Fe(CN)_6]$ up to $x = 0.4$ M. We evaluated κ ($\approx$0.5 W Km^{-1}) at 0.8 M by extrapolation. Thus, we obtained $ZT = 0.007$ in the LTE composed of the graphite-dispersing electrode at 298 K. In Table 3, we compare thus obtained ZT with those of ferro/ferri LTEs reported in literature. We note that R strongly depends on d, since R_s is proportional to d while R_{ct} and R_{dif} are independent on d.[27,28] The ZT values of our LTEs fall within the intermediate range among previously reported values.

4 Conclusions

We investigated the resistivity components in ferro/ferri LTE composed of graphite-dispersing electrodes against t. R_{ct}^{-1} and R_{dif}^{-1} linearly increase with t in the thin t region ($t \leq 40$ μm) reflecting the increase in electrochemical active surface area (EASA). Analysis of the EIS data at low f reveals that mass transfer process is the main rate-limiting factor in ferro/ferri LTE. W_{max} of the ferro/ferri LTE ($t = 97$ μm) reaches 0.76 W m^{-2} at $\Delta T = 50$ K, suggesting the effectiveness of the graphite-dispersing electrode in ferro/ferri LTE.

Author contributions

Soshi Fukuda: data curation; formal analysis; investigation. Yutaka Moritomo: conceptualization; supervision; and writing – original draft; writing – review & editing.

Conflicts of interest

There are no conflicts to declare.

Data availability

The data supporting this article will be provided if requested to the corresponding author.

Acknowledgements

This work was supported by supported by JSPS KAKENHI (Grant Number 25K01674), Panac Foundation, and joint research with Taisei Rotec Corporation.

Notes and references

1 T. Ikeshoji, Thermoelectric conversion by thin-layer thermogalvanic cells with soluble redox couples, *Bull. Chem. Soc. Jpn.*, 1987, **60**, 1505–1514.
2 I. Quickenden and Y. Mua, A review of power generation in aqueous thermogalvanic cells, *J. Electrochem. Soc.*, 1995, **142**, 3985.
3 Y. Mua and T. I. Quickenden, Power conversion efficiency, electrode separation, and overpotential in the ferricyanide/ferrocyanide thermogalvanic cell, *J. Electrochem. Soc.*, 1996, **143**, 2558.
4 J. Kawamura, M. Shimoji and H. Hoshino, The ionic conductivity and thermoelectric power of the superionic conductor Ag_3SBr, *J. Phys. Soc. Jpn.*, 1981, **50**, 194–200.
5 A. Schiraldi, E. Pezzati and P. Baldini, Thermoelectric power of the high ionic conductivity glasses silver iodide $AgI:Ag_2O{\cdot}B_2O_3$, *J. Phys. Chem.*, 1985, **89**, 1528–1531.
6 Y. Liang, J. K.-H. Hui, M. Morikawa, H. Inoue, T. Yamada and N. Kimizuka, High positive Seebeck coefficient of aqueous I^-/I^{3-} thermocells based on host-guest interactions and LCST behavior of PEGylated α-cyclodextrin, *Appl. Energy Metter.*, 2021, **4**, 5326–5331.
7 B. Yu, J. Duan, H. Cong, W. Xie, R. Liu, X. Ahuang, H. Wang, B. Qi, M. Xu and L. Wan, Thermosensitive crystallization–boosted liquid thermocells for low-grade heat harvesting, *Science*, 2020, **370**, 342–346.
8 Y. Xaing, X. Guo, H. Zhu, Q. Zhang and S. Zhu, Aqueous biphase-boosted liquid-state thermocell for continuous low-grade heat harvesting, *Chem. Eng. J.*, 2023, **461**, 142013.
9 J. H. Kim, J. H. Lee, E. E. Palen, M.-S. Suh, H. H. Lee and R. J. Kang, Iron (II/III) perchlorate electrolytes for electrochemically harvesting low-grade thermal energy, *Sci. Rep.*, 2019, **9**, 8706.
10 J. Duan, G. Feng, B. Yu, J. Li, M. Chen, P. Yang, J. Feng, K. Liu and J. Zhou, Aqueous thermogalvanic cells with a high Seebeck coefficient for low-grade heat harvest, *Nat. Commun.*, 2018, **9**, 5146.
11 T. Kim, J. S. Lee, G. Lee, H. Yoon, J. Yoon, T. J. Kang and Y. H. Kim, High thermopower of ferri/ferrocyanide redox couple in organic-water solutions, *Nano Energy*, 2017, **31**, 160.
12 M. Sindhuja, B. Lohith, V. Sudha, G. R. Manjunath and S. Harinipriya, Low grade thermal energy harvester using graphene-based Thermocells, *Mater. Res. Express*, 2017, **4**, 075513.
13 H. Im, T. Kim, H. Song, J. Choi, J. S. Park, R. Ovalle-Robles, H. D. Yang, K. D. Kihm, R. H. Baughman, H. H. Lee, T. J. Kang and Y. H. Kim, High-efficiency electrochemical thermal energy harvester using carbon nanotube aerogel sheet electrodes, *Nat. Commun.*, 2016, **7**, 10600.

14 H. Zhou, T. Yamada and N. Kimizuka, Supramolecular thermo-electrochemical cells: Enhanced thermoelectric performance by host–guest complexation and salt-induced crystallization, *J. Am. Chem. Soc.*, 2016, **138**, 10502–10507.
15 A. H. Kazim and B. A. Cola, Electrochemical characterization of carbon nanotube and poly (3,4-ethylenedioxythiophene) poly(styrenesulfonate) composite aqueous electrolyte for thermo-electrochemical cells, *J. Electrochem. Soc.*, 2016, **163**, F867.
16 S. W. Lee, Y. Yang, H.-W. Lee, H. Ghasemi, D. Kraemer, G. Chen and Y. Cui, An electrochemical system for efficiently harvesting low-grade heat energy, *Nat. Commun.*, 2014, **5**, 3942.
17 Y. Tanaka, A. Wake, D. Inoue and Y. Moritomo, Concentration gradient effect in liquid thermoelectric device composed of organic-solvent-added aqueous solution containing $K_4[Fe(CN)_6]/K_3[Fe(CN)_6]$, *Jpn. J. Appl. Phys.*, 2024, **63**, 014002.
18 A. Wake, D. Inoue and Y. Moritomo, A liquid thermoelectric device composed of organic solution, *Appl. Phys. Express*, 2022, **15**, 054002.
19 A. Wake, D. Inoue and Y. Moritomo, Liquid thermoelectric conversion devices composed of several organic solvents, *Jpn. J. Appl. Phys.*, 2023, **62**, 014002.
20 K. Kim, S. Hwang and H. Lee, Unravelling ionic speciation and hydration structure of Fe(III/II) redox couples for thermoelectrochemical cells, *Electrochem. Acta*, 2020, **335**, 135651.
21 M. A. Buckingham, F. Marken and L. Aldous, The thermoelectrochemistry of the aqueous iron(II)/iron(III) redox couple: significance of the anion and pH in thermogalvanic thermal-to-electrical energy conversion, *Sustain. Energy Fuels*, 2018, **2**, 2717–2726.
22 S.-M. Jung, S.-Y. Kang, B.-J. Lee, J. Kwon, D. Lee and Y.-T. Kim, Fe-N-C electrocatalyst for enhancing Fe(II)/Fe(III) redox kinetics in thermo-electrochemical cells, *Adv. Funct. Matter.*, 2023, **33**, 2304067.
23 B. Yu, H. Xiao, Y. Zeng, S. Liu, D. Wu, P. Liu, J. Guo, W. Xie, J. Duan and J. Zhou, Cost-effective n-type thermocells enabled by thermosensitive crystallizations and 3D multi-structured electrodes, *Nano Energy*, 2022, **93**, 106795.
24 J. H. Kim and T. J. Kang, Diffusion and Current Generation in Porous Electrodes for Thermo-electrochemical Cells, *Appl. Mater. Sci.*, 2019, **11**, 28894–28899.
25 W. Li, C. Gao, J. Ma, J. Qiu and S. Wang, Simultaneous enhancement of thermopower and ionic conductivity for N-type Fe(II/III) thermocell, *Mater. Today Energy*, 2022, **30**, 101147.
26 A. J. Bard, L. R. Faulkner and H. S. White, *Electrochemical Methods*, Wiley, West Sussex, 2022.
27 T. Aiba, D. Inoue and Y. Moritomo, Coated electrodes for liquid thermoelectric conversion devices to enhance Fe^{2+}/Fe^{3+} redox kinetics, *Sustain. Energy Fuels*, 2024, **8**, 2138–2143.
28 T. Aiba, H. Yamada and Y. Moritomo, Methanol-based thermoelectric conversion device with high power, *Indust. Chem. Mater.*, 2024, **3**, 223–230.
29 D. Inoue and Y. Moritomo, Concentration dependence of resistance components in solutions containing dissolved Fe^{2+}/Fe^{3+}, *RSC Adv.*, 2024, **14**, 6292–6297.
30 S. Castro-Ruiz and J. Garcia-Canadas, Impedance spectroscopy analysis of a thermoelectrochemical cell under operating conditions, *International Workshop on Impedance Spectroscopy (IWIS)*, 2022, p. 25, DOI: **10.1109/IWIS57888.2022.9975126**.
31 P. Connor, J. Schuch, B. Kaiser and W. Jaegermann, The determination of electrochemical active surface area and specific capacity revisited for the system MnO_x as an oxygen evolution catalyst, *Z. Phys. Chem.*, 2020, **234**, 979–994.
32 R. Martínez-Hincapié, J. Wegner, M. U. Anwar, A. Raza-Khan, S. Franzka, S. Kleszczynski and V. Colic, The determination of the electrochemically active surface area and its effects on the electrocatalytic properties of structured nickel electrodes produced by additive manufacturing, *Electrochim. Acta*, 2024, **476**, 143663.
33 H. Tian, C. Chen, Z. Yu, W. Luo, X. Yu, Z. Chang, S. Li, X. Cui and J. Shi, Controlled construction of core-shell structured Prussian blue analogues towards enhanced oxygen reduction, *ChemSusChem*, 2024, **17**, e202301265.
34 Y. Fukuzumi, Y. Hinuma and Y. Moritomo, Configuration entropy effect on temperature coefficient of redox potential of P2-Na_xCoO_2, *Jpn. J. Appl. Phys.*, 2019, **58**, 065501.